crystals

MDPI

Article

One-Step Fabrication for $CsPbBr_3$ Perovskite Thin Film via a Facile Ion-Solution Spraying Approach

Jin Chen [1], Jinpeng Xu [1], Yu Sun [1,*], Fengchao Wang [1], Jing Yang [1,*], Yunchen Dou [2], Canyun Zhang [1] and Jinfang Kong [1]

[1] College of Sciences, Shanghai Institute of Technology, 100 Haiquan Road, Shanghai 201418, China; jinchenxl@sit.edu.cn (J.C.); 226181131@mail.sit.edu.cn (J.X.); fcwang@sit.edu.cn (F.W.); zhang_canyun@sit.edu.cn (C.Z.); jfkong@sit.edu.cn (J.K.)

[2] School of Materials Science and Engineering, Shanghai Institute of Technology, 100 Haiquan Road, Shanghai 201418, China; yunchendou@sit.edu.cn

* Correspondence: yusunw@sit.edu.cn (Y.S.); yangjingxqq@sit.edu.cn (J.Y.); Tel.: +86-21-60873193 (Y.S. & J.Y.)

Abstract: In the current work, a facile ion-solution spraying strategy was employed for one-step fabrication of $CsPbBr_3$ perovskite thin films under atmosphere. The dependences of sample properties on annealing parameters (toleration temperature and duration time) were investigated in detail. As the results suggested, the sample prepared at 200 °C for 15 min featured better properties than others. The sample displayed a cubic phase with good crystallinity, a dense and compact morphology, a bandgap energy of 2.289 eV, and an average decay lifetime of 55.536 ns. Furthermore, the sample presented a Br-rich state, which was favorable for the carrier behavior and structure stability.

Keywords: spraying; annealing; thin film; $CsPbBr_3$ perovskite

Citation: Chen, J.; Xu, J.; Sun, Y.; Wang, F.; Yang, J.; Dou, Y.; Zhang, C.; Kong, J. One-Step Fabrication for $CsPbBr_3$ Perovskite Thin Film via a Facile Ion-Solution Spraying Approach. *Crystals* **2024**, *14*, 604. https://doi.org/10.3390/cryst14070604

Academic Editor: Francisco M. Morales

Received: 14 May 2024
Revised: 7 June 2024
Accepted: 27 June 2024
Published: 29 June 2024

1. Introduction

Nowadays, lead halide perovskite is considered a promising candidate for the applications of solar cells [1], lighting [2], lasers [3], display techniques [4], in sensors [5], and the biomedicine area [6], because of its excellent features of a high absorption coefficient [7], tunable bandgap [8], and good carrier mobility [9]. Tobias et al. investigated the optical properties of $CsPbBr_3$ perovskite organic multiple quantum wells and confirmed their potential as high-efficiency LED and laser sources [10]. Park et al. controlled the crystallization and surface morphology of α-form formamidine lead iodate ($FAPbI_3$) perovskite films by adding volatile alkyl ammonium chloride, achieving control over the growth of perovskite layer crystals and improving the efficiency of perovskite solar cells [11]. In 2024, Li et al. [12] used acid etching-driven nano surface reconstruction to reconstruct perovskite quantum dots ($CsPbI_3$ QDs) on the nano surface, resulting in highly efficient and stable red LED displays. Currently, the hybrid organic–inorganic perovskites (CH_3NHPbX_3, $CH(NH_2)_2PbX_3$, X=Cl, Br, I) are in prevalence, and the recorded power conversion efficiency (PCE) of photovoltaic devices is up to 26% [13]. However, the poor heating and moisture stability, which were caused by the volatility of organic cations (CH_3NH^{3+}, $CH(NH_2)^{2+}$), is the tricky issue for these hybrid ones [14]. Compared to the abovementioned organic–inorganic perovskites, all-inorganic perovskites showed great stability due to their higher structure tolerance, especially in $CsPbX_3$ material. This was desirable for the fabrication of high-performance photovoltaic devices [15].

Nowadays, devised methods, such as spin coating [16,17], co-evaporation [18,19], gas-phase-assisted solution [20], and nanocrystals (NCs) coating [21] have been employed for the fabrication of perovskite thin films. The co-evaporation and the gas-phase-assisted deposition method belong to vacuum technology. Ma et al. [22] employed the co-evaporation method to prepare a $CsPbBr_3$ photon-harvesting layer, and the PCE of the device was 4.7%. Patil et al. reported the fabrication of this perovskite material by the gas-phase-assisted

method, and gained a device PCE of 16.45% [23]. Unfortunately, these vacuum methods were restricted by their high energy consumption and complicated operation. Spin coating and NCs coating were the typical non-vacuum avenues for the fabrication. Wu et al. prepared the perovskite solar cells by spin coating, and the PCE of the fabricated device was 16.07% [24]. In 2021, Hu et al. reported an 8.1% PCE for the device which was fabricated via the strategy of NCs coating [25]. However, the spin coating had poor repeatability and was not suitable for large-area production, and the NCs coating was complicated and time consuming which was caused by the synthesis process.

Concerning the issues of the above methods, the spraying approach, which features facile operation, low time-consumption, and scalable production, may be an effective dissolution strategy. Currently, it has been widely employed for the fabrication of binary and multiple compounds. Yang et al. reported their work on the deposition of $CsPbBr_3$ thin film by the spraying approach based on $CsPbBr_3$ NCs for the first time [26]. Wang [27] et al. first dissolved CsBr and $PbBr_2$ in a DMF solution, then added oleic acid (OA) and oleyl amine (OLA) as ligands, and then placed the above solution in a centrifuge at 8000 rpm for 10 min to remove the residue to obtain a transparent precursor solution. Finally, luminescent $CsPbBr_3$ thin films were prepared by the spraying method. The Park team used dimethyl sulfoxide (DMSO) and N,N-dimethylformamide (DMF) as solvents to prepare $CsPbBr_3$ precursor solutions, and then sprayed thin films on a substrate at 150 °C. The crystal size of $CsPbBr_3$ was controlled by adjusting the concentration ratio of DMSO/DMF [28].

Differing from the abovementioned work, a one-step deposition strategy for $CsPbBr_3$ perovskite thin films via the spraying approach with ion-solution was displayed in our current work. To our knowledge, similar reports have been rarely reported to date. Moreover, the effects of annealing parameters (toleration temperature and duration time) on the structural, compositional, morphological, and optical performances of fabricated $CsPbBr_3$ thin films were investigated in detail. The purpose of the present work is to provide a new possibility for the facile and high-performance fabrication of $CsPbBr_3$ thin films, which is desired for photovoltaic devices.

2. Experimental

2.1. Fabrication of $CsPbBr_3$ Thin Films by the Ion-Solution Spraying Method

Typically, 0.2 mmol CsBr (cesium bromide, 99%, AR) and 0.2 mmol $PbBr_2$ (lead bromide, 99%, AR) were successively dissolved in 20 mL DMSO (dimethyl sulfoxide, 90%) to prepare the ion-solution. The stoichiometric ratio of Cs:Pb:Br was 1:1:3. The magnetic stirring was carried out for the sufficient dissolution under room temperature. Then, this solution was placed into a spray gun, and deposited on the heating glass-substrate to obtain the precursor thin films. Finally, the above thin films were annealed by a hot platform under atmosphere. Different annealing parameters including toleration temperature and duration time were employed. During the spraying process, the distance between the spray gun and the substrate was about 20 cm, and the inclination angle was 45 °. For the subsequent work, ITO conductive glass was used as the substrate in the experiment. The brief schematic diagram for the preparation process is shown in Figure 1.

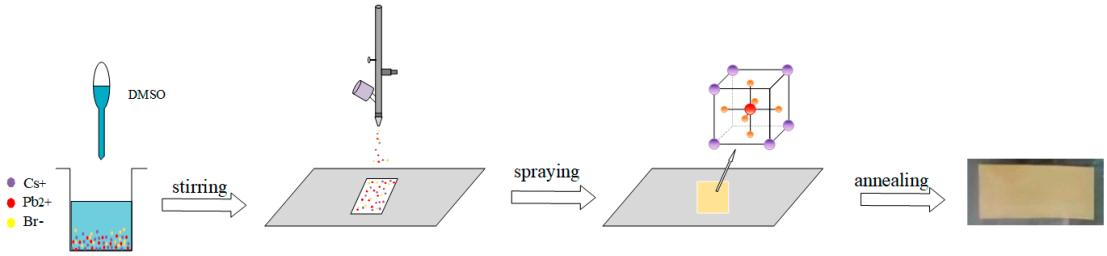

Figure 1. The schematic diagram of spraying process.

2.2. Characterizations for the As-Obtained Samples

The film's crystalline structure was characterized by X-ray diffraction (XRD, Ultima IV, Rigaku, Tokyo, Japan). The surface morphology was measured by scanning electron microscopy (SEM, Quanta 200, FEI, Eindhoven, Netherlands). The optical property of as-prepared samples was determined by an Ultraviolet-Visible-Infrared spectrophotometer (UV-vis-IR, UH 4150, Hitachi, Tokyo, Japan). Energy dispersive X-ray spectroscopy (EDS, Genesis Apollo X, EDAX, PA, USA) and X-ray photoelectron spectroscopy (XPS, Axis Ultra DLD, Kratos, Manchester, UK) were employed for the study of chemical constitution. All tests were carried out at room temperature.

3. Results and Discussion

3.1. Effects of Toleration Temperature on $CsPbBr_3$ Thin Films

Regarding the spraying method, the possible mechanism could be described as follows. In the first step, the bromides of CsBr and $PbBr_2$ were sufficiently dissolved in the polar solvent of DMSO to form the expected ion-solution. The dissolution process could be displayed in Equations (1) and (2). In this solution, Cs^+, Pb^{2+}, and Br^- ions were distributed isolatedly and homogeneously. In the second stage, the ion-solution was deposited onto the heating substrate. These ions would incorporate with each other to form $CsPbBr_3$ products by heating treatment with the evaporation of the solvent, which was depicted as Equation (3). In this stage, the yellow precursor film could be obtained. Successively, the annealing treatment was carried out to proceed with the reaction further.

$$CsBr \rightarrow Cs^+ + Br^- \quad (1)$$

$$PbBr_2 \rightarrow Pb^{2+} + 2Br^- \quad (2)$$

$$Cs^+ + Pb^{2+} + 3Br^- \rightarrow CsPbBr_3 \quad (3)$$

To observe the effect of the annealing temperature on the properties of $CsPbBr_3$ thin films, the temperatures were varied at a 175~250 °C range with an increment of 25 °C. The duration time was 10 min. The XRD patterns of as-prepared samples at different toleration temperatures are shown in Figure 2a. The diffraction peaks locating at 15.21, 21.62, and 30.70° were separately attributed to (100), (110), and (200) planes of CsPbBr3 with cubic structure (JCPDS No 00-054-0752). As seen in Figure 2a, the intensity of the diffraction peak showed an upward trend with the annealing temperature at 175~200 °C, which indicated an improving crystallinity. When the temperature was over 200 °C, the crystallinity deteriorated as the temperature increased. As previously reported [29], when the temperature was low, the decomposition of solvent volatiles was slow, and the growth rate of crystals was slow. However, when the temperature was too high, the solvent evaporates rapidly and the crystal growth was insufficient, resulting in a decrease in grain size. It was observed that the shape of these peaks changed as the temperature varied. These changes could be described by full width at half maximum (FWHM). After 200 °C, the value of FWHM increased when the toleration temperature rose. According to the Scherrer formula [30] ($D = k\lambda/\beta\cos\theta$, where D is the grain size, k is a constant, λ is the Cu Kα wavelength (0.15406 nm), β is the value of FWHM, and θ is the diffraction angle), the grain size was inversely proportional to FWHM. The error lines for FWHM and crystal size of the samples prepared at different annealing temperature are shown in Figure 2b. It was noted that the 200 °C sample had the largest crystal size compared with the others.

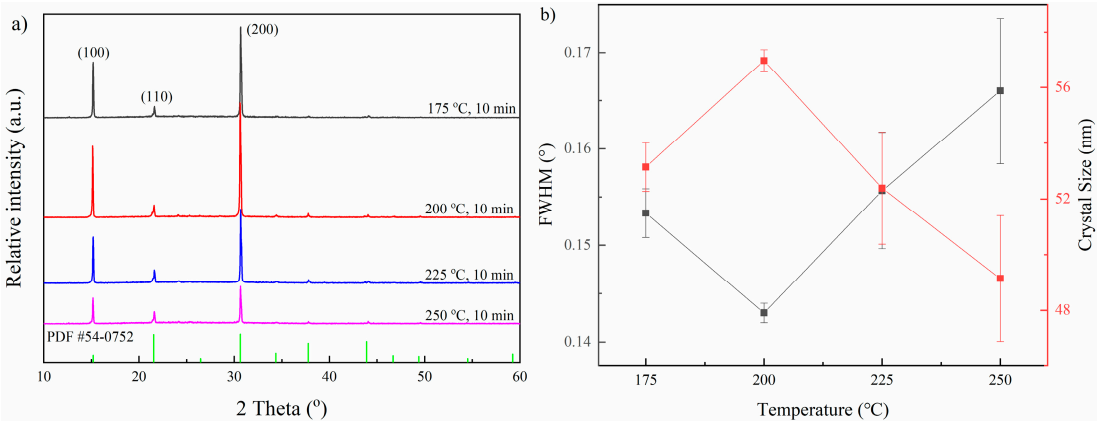

Figure 2. (**a**) XRD pattern and (**b**) the error lines for FWHM and crystal size of the samples prepared at different toleration temperatures.

Figure 3 shows the surface morphologies of as-obtained $CsPbBr_3$ thin films fabricated at different annealing temperatures. As observed in Figure 3a–d, the products on the surface were in an angular strip-bulk shape without cracks and holes, meanwhile, these films featured compact and dense. This morphology may facilitate carrier migration, which is desirable for high-performance photovoltaic devices. It was noted that the size of the bulk products at 200 °C was larger than the other samples. In addition, it was also found that the organics from the used solvent could be evaporated as well.

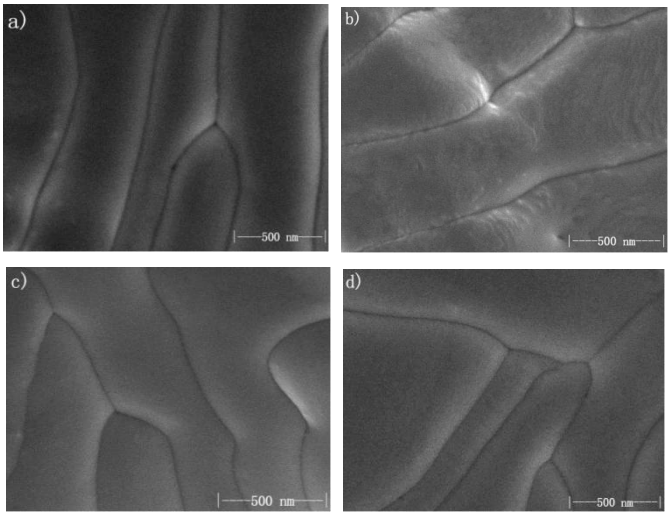

Figure 3. Morphologies of the samples prepared at different temperatures: (**a**) 175 °C, (**b**) 200 °C, (**c**) 225 °C, (**d**) 250 °C.

The absorption spectra of as-prepared samples are displayed in Figure 4a. For $CsPbBr_3$ material, the conduction band minimum (CBM) was mostly occupied by Pb-6p orbitals, while the valence band maximum (VBM) with antibonding features was mainly consisted of Br-4p orbitals. The transition from the valence band to the conduction band determined the optical properties of $CsPbBr_3$ in the visible region [31]. As observed, these annealed samples all presented a clear absorption edge. The absorption edge steepened as the annealing temperature increased in the 175~200 °C range, which indicated the crystallinity improved. However, the steepness decreased with the increasing temperature in the 200~250 °C range. This was consistent with XRD analysis. The bandgap energy *Eg* of these samples was determined by extrapolating the straight line of $(Ahv)^2$ vs. (hv) plots as exampled in the inset of Figure 4b. Here, *A* is absorbance, *h* is Planck's constant, and *v* is frequency. As

observed, the error line of *Eg* value variation is shown in Figure 4b. When the annealing temperature was 200 °C, the *Eg* value was 2.262 eV.

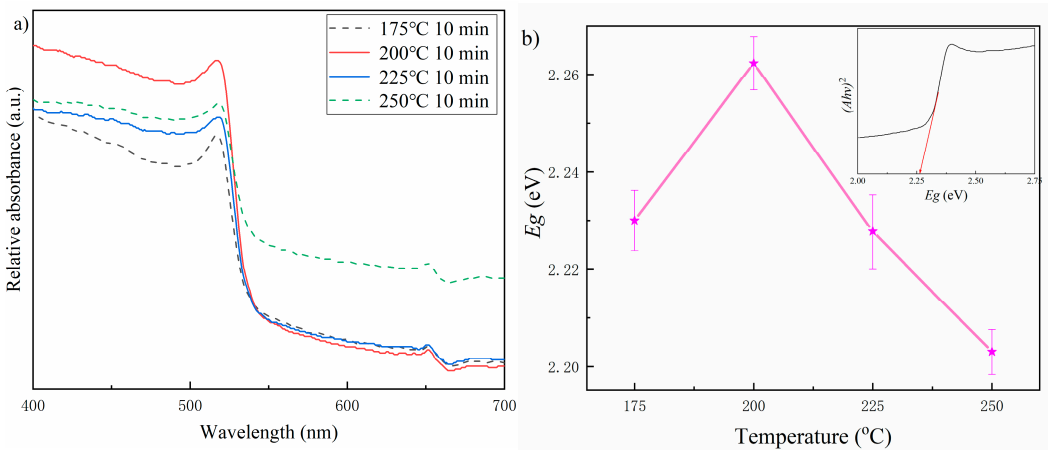

Figure 4. (**a**) Absorption spectra and (**b**) error lines of $(Ahv)^2$ vs. (hv) of the samples prepared at different temperatures.

As above analyzed, the 200 °C sample featured better crystallinity, morphology, and optical property compared with other samples. This suggested the annealing temperature of 200 °C was promising for the next investigation.

3.2. Effects of Duration Time on $CsPbBr_3$ Thin Films

Here, the annealing time was changed to a 5~20 min range with intervals of 5 min to examine the property variations of the prepared samples. The annealing temperature was set to 200 °C as above suggested. Figure 5a displays the XRD patterns of the samples undertaken by different duration times. As seen, the diffraction peaks at 15.21, 21.62, and 30.70° were attributed to (100), (110), and (200) planes of cubic $CsPbBr_3$, respectively. It was noted that the absence of impurity suggested the obtained product was in the pure phase. It was found that the peak intensity increased as the time prolonged in 5~15 min, which indicated an improving crystallinity and crystal size. Unfortunately, the continued extension of annealing time led to the decomposition of thin film grains, resulting in a decrease in crystallinity and grain size. A similar phenomenon was also reported in previous work [32]. The error lines for FWHM and crystal size of the samples prepared at different annealing times are shown in Figure 5b. The FWHM showed a downward trend in the 5~15 min range, and an upward variation when the annealing time was over 15 min. This was consistent with the shape changes of diffraction peaks. According to the Scherrer formula, FWHM and grain size were inversely proportional. When the annealing time was 15 min, the FWHM of the prepared sample was the smallest and the grain size was the largest.

The surface morphology of the samples prepared at different annealing times is shown in Figure 6. When the annealing time was 5 min, the holes appeared on the sample surface and disappeared during the 10~20 min range. This may be attributed to the product growing as the annealing time increased. As seen, the morphology of these samples was dense and compact. The stripped products on the film surface presented as bulk-state, which is favorable for carrier migration. Regarding the 15 min sample, the largest size of the bulk products could be over 500 nm.

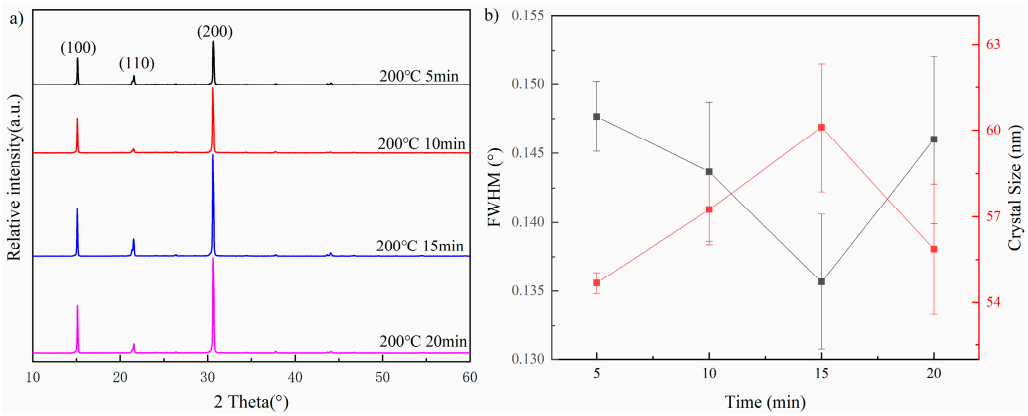

Figure 5. (**a**) XRD pattern and (**b**) the error lines for FWHM and crystal size of the samples prepared at different duration times.

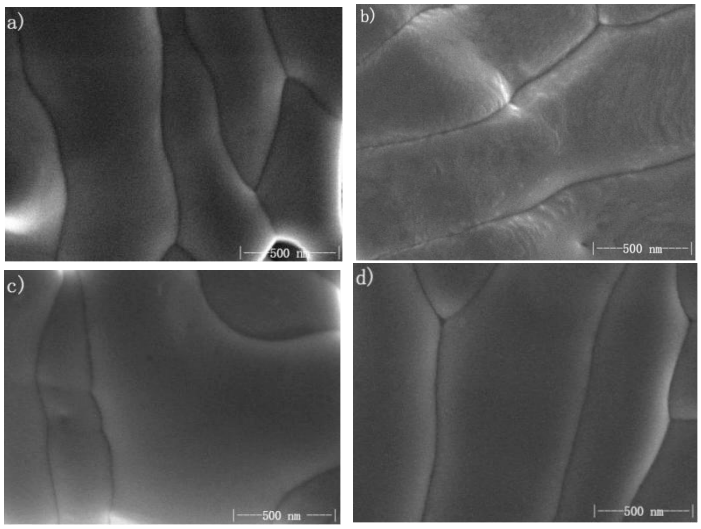

Figure 6. Morphologies of the samples prepared at different times: (**a**) 5 min, (**b**) 10 min, (**c**) 15 min, (**d**) 20 min.

The optical properties of $CsPbBr_3$ thin films prepared at different duration times are shown in Figure 7. Figure 7a shows the absorption spectra of the obtained samples, while the transmission mode was conducted here. All the samples featured a cut-off absorption edge. For the 15 min sample, it had the steepest cut-off edge for the absorption spectrum, which can be attributed to the best crystallinity as suggested by XRD analysis. Figure 7b shows the error line of *Eg* values variation. As observed, the *Eg* presented an upward trend in the 5~10 min range and declined when the duration time was prolonged to 20 min. The *Eg* value of the thin film prepared under annealing of 200 °C and 15 min was 2.289 eV.

According to the above analyses, the properties of the films prepared at 200 °C for 15 min were better than those of the other samples. As suggested by previous work [33], the carrier lifetime was one of the key factors for photovoltaic devices. Figure 8 shows the time-resolved fluorescence decay curves of $CsPbBr_3$ films at 200 °C for 15 min. The curves could be fitted by a bi-exponential function as shown in Equation (4) [34]:

$$y = A_0 + A_1 \exp\left(-\frac{t}{\tau_1}\right) + A_2 \exp\left(-\frac{t}{\tau_2}\right) \quad (4)$$

$$\tau_{ave} = \left(A_1\tau_1^2 + A_2\tau_2^2\right)/\left(A_1\tau_1 + A_2\tau_2\right) \quad (5)$$

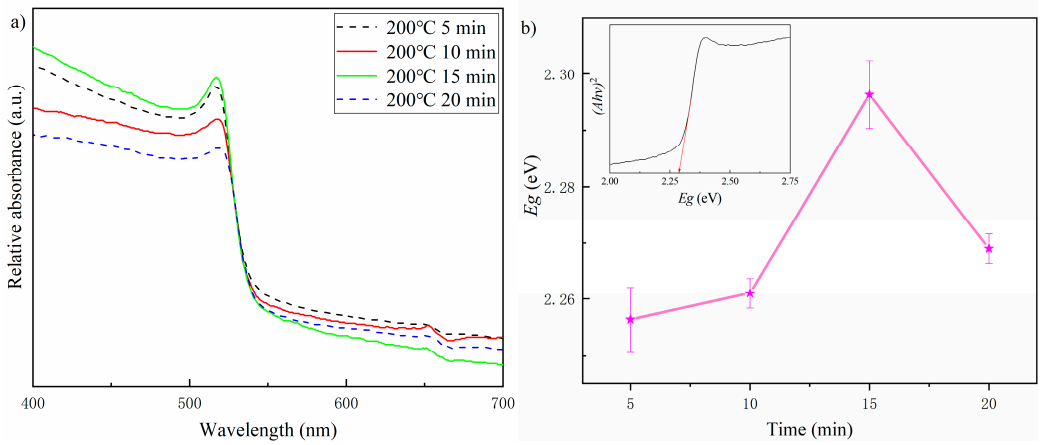

Figure 7. (**a**) Absorption spectra and (**b**) error lines of $(Ahv)^2$ vs. (hv) of the samples prepared at different times.

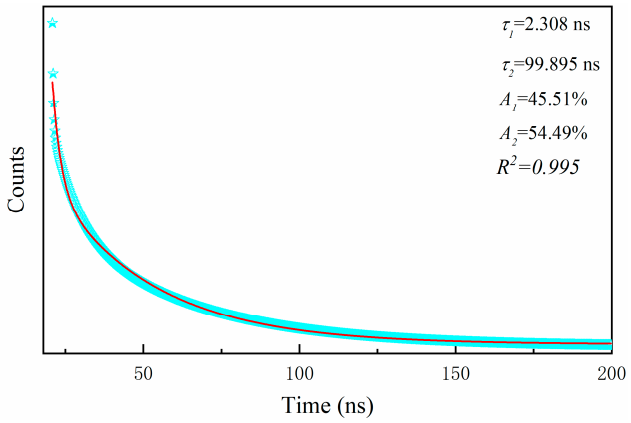

Figure 8. PL lifetime of samples prepared at 200 °C for 15 min.

Here, τ_1 is the fast decay component which reflects the no-radiative recombination process resulting from the defects, τ_2 is the slow decay component relating to the trap-assisted radiative process in the bulk perovskite. A_1 and A_2 are the corresponding fractional amplitudes of τ_1 and τ_2, respectively. A_0 is a constant. In addition, the average lifetime τ_{ave} is calculated by Equation (5). For the obtained samples, the τ_1 value was 2.308 ns, τ_2 value was 99.895 ns, and their corresponding A_1 and A_2 values were 45.51% and 54.49%, respectively. The calculated τ_{ave} value was 55.536 ns. This indicated the sample had a good carrier migration behavior which was beneficial to separate the free electron from the hole effectively as suggested by previous work [33]. The value of the statistical indicator R^2 was 0.995, which was very close to 1, indicating that the model used had a good fitting effect.

In order to better characterize the performance of the thin film, the SEM cross-sectional image of the prepared sample is shown in Figure 9a. The thickness of the prepared sample is 3.7 μm. In the future, the preparation process could be further improved to make the film thickness thinner. Furthermore, the chemical composition of this sample was determined by EDS. As shown in Figure 9b, the atomic percent of Cs:Pb:Br was 1:0.89:3.03. The Pb/(Cs+Br) ratio was 0.22, which suggested a Pb-poor state of the synthesized sample resulting from the poor solubility of the Pb source in the reaction solution [35]. The Br/(Cs+Pb) ratio was around 1.6. This indicated the sample was in a Br-rich state. As suggested by previous studies [36], the Br-rich state could facilitate the reduction of Br vacancies, which is favorable for the carrier behavior. In addition, this chemical composition was also beneficial for the structure stability of the prepared sample [35].

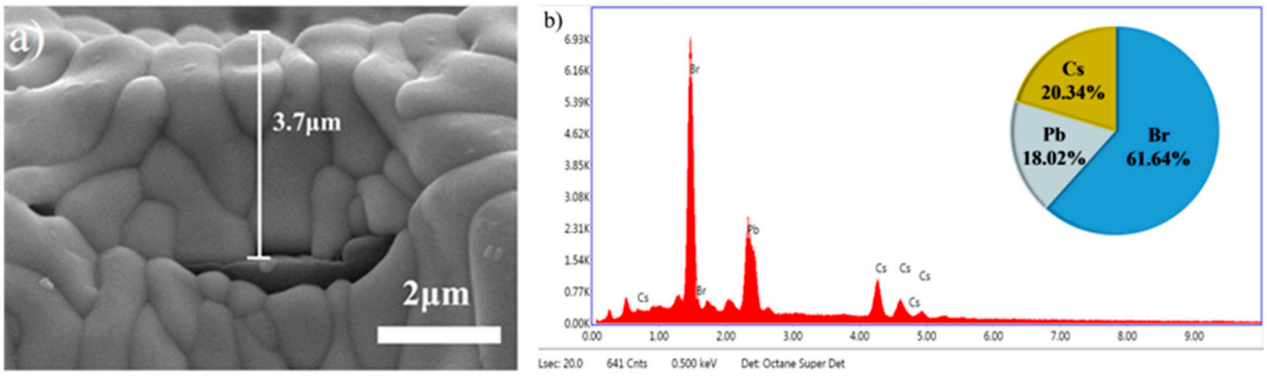

Figure 9. The samples prepared at 200 °C for 15 min: (**a**) SEM cross-sectional images and (**b**) chemical composition.

The composition of the obtained sample prepared under the condition of 200 °C for 15 min was further investigated by XPS observation. The full spectrum of XPS is shown in Figure 10a. It was found that the spectrum of each element had double detected peaks of self-spin orbit splitting, which resulted from the spin orbit coupling [31]. As Figure 10b displays, the peaks located at 723.29 eV and 737.38 eV correspond to Cs $3d_{5/2}$ and Cs $3d_{3/2}$, respectively. The splitting space was 13.9 eV. This indicated Cs was univalent. For Pb, two characteristic peaks of 137.26 eV and 142.11 eV with a separation of 4.85 eV were observed as shown in Figure 10c. These two peaks were attributed to Pb $4f_{7/2}$ and Pb $4f_{5/2}$, respectively. This confirmed the existence of bivalent Pb. Two different binding states of 68.15 eV and 67.21 eV were obtained as shown in Figure 10d. It suggested two different chemical environments of the Br element: the peak of 68.15 eV deriving from the high energy band of Pb-Br, and the peak of 67.21 eV originating from the low energy band of Cs-Br [21].

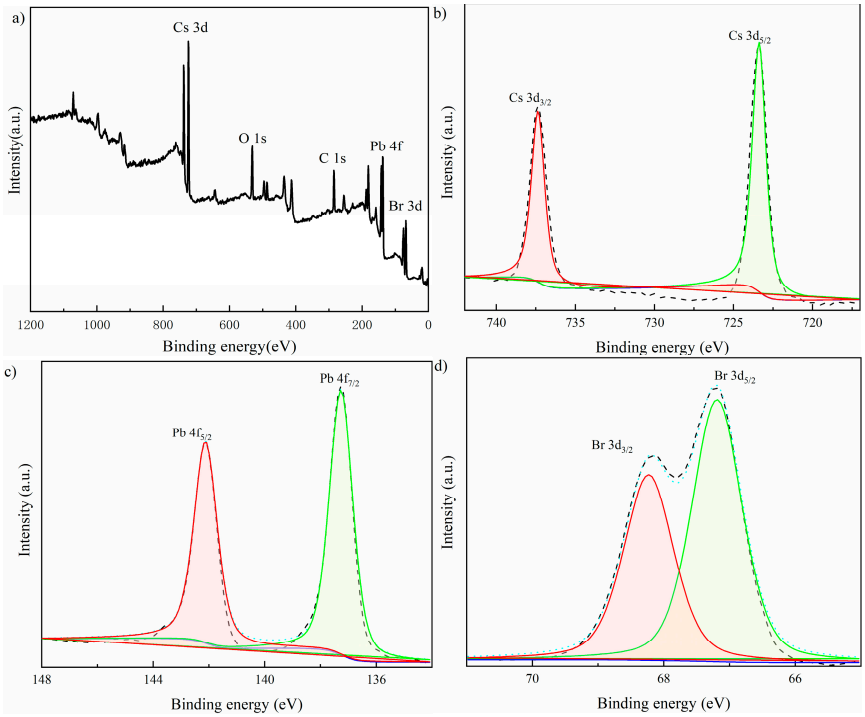

Figure 10. XPS spectrum of the obtained sample prepared at 200 °C for 15 min. (**a**) The full spectrum of XPS; (**b**) the peaks located at 723.29 eV and 737.38 eV correspond to Cs 3d5/2 and Cs 3d3/2, respectively; (**c**) Two characteristic peaks of 137.26 eV and 142.11 eV with a separation of 4.85 eV were observed; (**d**) Two different binding states of 68.15 eV and 67.21 eV were obtained.

4. Conclusions

In summary, we have successfully fabricated a $CsPbBr_3$ thin film based on the facile spraying approach under atmosphere. The intrinsic relationship between annealing parameters (toleration temperature and duration time) and the samples' properties was investigated in detail. As the results show, the best sample could be obtained under the condition of 200 °C for 15 min. The sample featured a good crystallinity with a cubic structure, a dense and compact surface morphology, and a bandgap energy of 2.289 eV. The PL lifespan was obtained through fitting, the τ_1 value was 2.308 ns, the τ_2 value was 99.895 ns, and their corresponding A_1 and A_2 values were 45.51% and 54.49%, respectively. The calculated τ_{ave} value was 55.536 ns. Moreover, the fabricated sample was in a Br-rich state, which was favorable for the carrier behavior and structure stability. Finally, the XPS spectrum confirmed the composition of the prepared sample and the binding energy of different elements. In future work, the as-fabricated $CsPbBr_3$ thin film will be involved in the fabrication of photovoltaic devices.

Author Contributions: Conceptualization, J.C.; Data curation, Y.D.; Formal analysis, J.C. and Y.S.; Funding acquisition, J.C., F.W. and J.Y.; Investigation, J.X. and J.K.; Methodology, J.Y.; Project administration, F.W.; Software, J.Y. and C.Z.; Supervision, F.W. and C.Z.; Validation, J.X. and Y.S.; Visualization, Y.D. and J.K.; Writing—original draft, Y.S.; Writing—review and editing, J.C. and Y.S. All authors have read and agreed to the published version of the manuscript.

Funding: This research was funded by [the Shanghai Sailing Program] grant number [20YF1447600 and No. 18YF1422500]. And the research was funded by [Start-up Project of the Shanghai Institute of Technology] grant number [YJ2021-60]. This research was funded by [the Collaborative Innovation Project of the Shanghai Institute of Technology] grant number [XTCX2020-12 and No. XTCX2023-22], and [the Science and Technology Talent Development Fund for Young and Middle-Aged Teachers of the Shanghai Institute of Technology] grant number [ZQ2022-6].

Data Availability Statement: The data presented in this study are available on request from the corresponding author due to privacy.

Conflicts of Interest: The authors declare no conflicts of interest.

References

1. Lee, M.M.; Teuscher, J.; Miyasaka, T.; Murakami, T.N.; Snaith, H.J. Efficient hybrid solar cells cased on meso-superstructured organometal halide perovskites. *Science* **2012**, *338*, 643–647. [CrossRef] [PubMed]
2. Zhang, L.Q.; Yang, X.L.; Jiang, Q.; Wang, P.Y.; Yin, Z.G.; Zhang, X.W.; Tan, H.; Yang, Y.M.; Wei, M.Y.; Sutherland, B.R.; et al. Ultra-bright and highly efficient inorganic based perovskite light-emitting diodes. *Nat. Commun.* **2017**, *8*, 15640. [CrossRef] [PubMed]
3. Wang, Y.; Li, X.; Song, J.; Xiao, L.; Zeng, H.; Sun, H. All inorganic colloidal perovskite quantum dots: A new class of lasing materials with favorable characteristics. *Adv. Mater.* **2015**, *27*, 7101–7108. [CrossRef] [PubMed]
4. Dai, S.-W.; Hsu, B.-W.; Chen, C.-Y.; Lee, C.-A.; Liu, H.-Y.; Wang, H.-F.; Huang, Y.-C.; Wu, T.-L.; Manikandan, A.; Ho, R.-M.; et al. Perovskite quantum dots with near unity solution and neat-film photoluminescent quantum yield by novel spray synthesis. *Adv. Mater.* **2018**, *30*, 1705532. [CrossRef] [PubMed]
5. Ollearo, R.; Ma, X.; Akkerman, H.B.; Fattori, M.; Dyson, M.J.; van Breemen, A.J.J.M.; Meskers, S.C.J.; Dijkstra, W.; Janssen, R.A.J.; Gelinck, G.H. Vitality surveillance at distance using thin-film tandem-like narrowband near-infrared photodiodes with light-enhanced responsivity. *Sci. Adv.* **2023**, *9*, 9861. [CrossRef] [PubMed]
6. Chen, Y.-H.; Kataria, M.; Hung, I.L.; Inbaraj, C.R.P.; Liao, Y.-M.; Hu, H.W.; Chang, T.-J.; Lu, C.-H.; Shih, W.-H.; Wang, W.-H.; et al. Ultrahighly photosensitive and highly stretchable rippled structure photodetectors based on perovskite nanocrystals and graphene. *ACS Appl. Electron. Mater.* **2019**, *1*, 1517–1526. [CrossRef]
7. Wolf, S.D.; Holovsky, J.; Moon, S.J.; Löper, P.; Niesen, B.; Ledinsky, M.; Haug, F.J.; Yum, J.H.; Ballif, C. Organometallic halide perovskites: Sharp optical absorption edge and its relation to photovoltaic performance. *J. Phys. Chem. Lett.* **2014**, *5*, 1035–1039. [CrossRef] [PubMed]
8. Noh, J.H.; Im, S.H.; Heo, J.H.; Mandal, T.N.; Seok, S.I. Chemical management for colorful, efficient, and stable inorganic-organic hybrid nanostructured solar cells. *Nano Lett.* **2013**, *13*, 1764–1769. [CrossRef] [PubMed]
9. Stoumpos, C.C.; Malliakas, C.D.; Kanatzidis, M.G. Semiconducting tin and lead iodide perovskites with organic cations: Phase transitions, high mobilities, and near-infrared photoluminescent properties. *Inorg. Chem. Commun.* **2013**, *52*, 9019–9038. [CrossRef]
10. Antrack, T.; Kroll, M.; Sudzius, M.; Cho, C.; Imbrasas, P.; Albaladejo-Siguan, M.; Benduhn, J.; Merten, L.; Hinderhofer, A.; Schreiber, F.; et al. Optical properties of perovskite-organic multiple quantum wells. *Adv. Sci.* **2022**, *9*, 2200379. [CrossRef]

11. Park, J.; Kim, J.; Yun, H.-S.; Paik, M.J.; Noh, E.; Mun, H.J.; Kim, M.G.; Shin, T.J.; Seok, S.I. Controlled growth of perovskite layers with volatile alkylammonium chlorides. *Nature* **2023**, *616*, 724–730. [CrossRef] [PubMed]
12. Li, H.; Feng, Y.; Zhu, M.; Gao, Y.; Fan, C.; Cui, Q.; Cai, Q.; Yang, K.; He, H.; Dai, X.; et al. Nanosurface-reconstructed perovskite for highly efficient and stable active-matrix light-emitting diode display. *Nat. Nanotechnol.* **2024**, *19*, 638–645. [CrossRef] [PubMed]
13. National Renewable Energy Laboratory, Best Research-Cell Efficiency Chart. 2024. Available online: https://www.nrel.gov/pv/cell-efficiency.html (accessed on 10 May 2024).
14. Rong, Y.G.; Liu, L.F.; Mei, A.Y.; Li, X.; Han, H.W. Beyond efficiency: The challenge of stability in mesoscopic perovskite solar cells. *Adv. Energy Mater.* **2015**, *5*, 1501066. [CrossRef]
15. Yang, B.; Chen, J.S.; Hong, F.; Mao, X.; Zheng, K.B.; Yang, S.Q.; Li, Y.J.; Pullerits, T.; Deng, W.Q.; Han, K. Lead-free, air-stable all-inorganic cesium bismuth halide perovskite nanocrystals. *Angew. Chem. Int. Ed.* **2017**, *56*, 12471–12475. [CrossRef] [PubMed]
16. Jeon, N.J.; Na, H.; Jung, E.H.; Yang, T.Y.; Lee, Y.G.; Kim, G.; Shin, H.W.; Seok, S.I.; Lee, J.; Seo, J. A fluorene-terminated hole-transporting material for highly efficient and stable perovskite solar cells. *Nat. Energy* **2018**, *3*, 682–689. [CrossRef]
17. Burschka, J.; Pellet, N.; Moon, S.J.; Humphry-Baker, R.; Gao, P.; Nazeeruddin, M.; Graetzel, M. Sequential deposition as a route to high-performance perovskite-sensitized solar cells. *Nature* **2013**, *499*, 316–319. [CrossRef] [PubMed]
18. Chen, Q.; Zhou, H.P.; Hong, Z.R.; Luo, S.; Duan, H.; Wang, H.; Liu, Y.S.; Li, G.; Yang, Y. Planar heterojunction perovskite solar cells via vapor-assisted solution process. *J. Am. Chem. Soc.* **2014**, *136*, 622–625. [CrossRef] [PubMed]
19. Lei, J.; Gao, F.; Wang, H.X.; Li, J.; Jiang, J.X.; Wu, X.; Gao, R.R.; Yang, Z.; Liu, S.Z. Efficient planar $CsPbBr_3$ perovskite solar cells by dual-source vacuum evaporation. *Sol. Energy Mater. Sol. Cells* **2018**, *187*, 1–8. [CrossRef]
20. Lin, Q.Q.; Armin, A.; Nagiri, R.C.R.; Burn, P.L.; Meredith, P. Electro-optics of perovskite solar cells. *Nat. Photonics* **2015**, *9*, 106–112. [CrossRef]
21. Woo, J.Y.; Kim, Y.; Bae, J.; Kim, T.G.; Kim, J.W.; Lee, D.C.; Jeong, S. Highly stable cesium lead halide perovskite nanocrystals through in situ lead halide inorganic passivation. *Chem. Mater.* **2017**, *29*, 7088–7092. [CrossRef]
22. Ma, Q.S.; Huang, S.J.; Wen, X.M.; Green, M.A.; Ho-Baillie, A.W.Y. Hole transport layer free inorganic $CsPbIBr_2$ perovskite solar cell by dual source thermal evaporation. *Adv. Energy Mater.* **2016**, *6*, 1502202. [CrossRef]
23. Patil, J.V.; Mali, S.S.; Hong, C.K. Efficient and stable all-inorganic niobium-incorporated $CsPbI_2Br$ based perovskite solar cells. *Acs Appl. Mater. Interfaces* **2020**, *12*, 27176–27183. [CrossRef] [PubMed]
24. Chen, W.J.; Chen, H.Y.; Xu, G.Y.; Xue, R.M.; Wang, S.H.; Li, Y.W.; Li, Y.F. Precise Control of crystal growth for highly efficient $CsPbI_2Br$ perovskite solar cells. *Joule* **2019**, *3*, 191–204. [CrossRef]
25. Hu, L.; Guan, X.W.; Chen, W.J.; Yao, Y.C.; Wan, T.; Lin, C.; Pham, N.D.; Yuan, L.; Geng, X.; Wang, F.; et al. Linking phase segregation and photovoltaic performance of mixed-halide perovskite films through grain size engineering. *ACS Energy Lett.* **2021**, *6*, 1649–1658. [CrossRef]
26. Yang, Z.; Wang, M.Q.; Li, J.J.; Dou, J.J.; Qiu, H.W.; Shao, J.Y. Spray-coated $CsPbBr_3$ quantum dot films for perovskite photodiodes. *ACS Appl. Mater. Interfaces* **2018**, *10*, 26387–26395. [CrossRef] [PubMed]
27. Wang, F.; Peng, X.; Wang, C.; Dong, H.; Sun, Y.; Kong, J.; Zhang, C.; Chen, J.; Li, L.; Xu, J. Synthesis of CsPbBr3 and CsPbBrXI(3−X) Films by Spray-Coating Technique. *ECS J. Solid. State Sci. Technol.* **2020**, *9*, 126007. [CrossRef]
28. Park, J.K.; Kim, S.Y.; Kim, J.H. Spray-coated nanocrystalline $CsPbBr_3$ perovskite thin-films for large area and efficient rigid and flexible light emitting diodes. *J. Alloys Compd. Interdiscip. J. Mater. Sci. Solid-State Chem. Phys.* **2022**, *918*, 165560. [CrossRef]
29. Gao, B.; Meng, J. High efficiently $CsPbBr_3$ perovskite solar cells fabricated by multi-step spin coating method. *Sol. Energy* **2020**, *211*, 1223–1229. [CrossRef]
30. Chen, J.; Chen, Q.M.; Ni, Y.; Yamaguchi, Y.; Wang, T.T.; Jia, Z.; Dou, X.M. The synthesis of Cu_2ZnSnS_4 nanoparticles via an open-air solution route: Influences of Zn precursor content. *J. Sol. Gel Sci. Technol.* **2015**, *75*, 25–30. [CrossRef]
31. Kim, M.; Kim, J.H.; Kim, M.; Kim, C.S.; Choi, J.W.; Choi, K.; Lee, J.H.; Park, J.; Kang, Y.; Jin, S.; et al. Enhanced photoluminescence quantum efficiency and stability of water assisted $CsPbBr_3$ perovskite nanocrystals. *J. Ind. Eng. Chem.* **2020**, *88*, 84–89. [CrossRef]
32. Bai, T.; Wang, S.; Zhang, K.; Chu, C.; Sun, Y.; Yi, L. High stability and strong luminescence $CsPbBr_3$-Cs_4PbBr_6 thin films for all-inorganic perovskite light-emitting diodes. *RSC Adv.* **2023**, *13*, 24413–24422. [CrossRef] [PubMed]
33. Zhang, X.; Gao, X.Y.; Meng, X. Fabrication and characterization of all-inorganic halide perovskite $CsPbBr_3$ films via the two-step sol-gel process: Impact of annealing temperature. *J. Alloys Compd.* **2019**, *810*, 151943. [CrossRef]
34. Bi, D.Q.; Yi, C.Y.; Luo, J.S.; Décoppet, J.; Zhang, F.; Zakeeruddin, S.M.; Li, X.; Hagfeldt, A.; Grätzel, M. Polymer-templated nucleation and crystal growth of perovskite films for solar cells with efficiency greater than 21%. *Nat. Energy* **2016**, *1*, 16142. [CrossRef]
35. Peng, X.G.; Chen, J.; Wang, F.C.; Zhang, C.Y.; Yang, B.B. One-pot synthesis of $CsPbBr_3/Cs_4PbBr_6$ perovskite composite. *Optik* **2020**, *208*, 164579. [CrossRef]
36. Zhang, X.S.; Jin, Z.W.; Zhang, J.R.; Bai, D.L.; Bian, H.; Wang, K.; Sun, J.; Wang, Q.; Liu, S.F. All-ambient processed binary $CsPbBr_3$-$CsPb_2Br_5$ perovskites with synergistic enhancement for high-efficiency Cs-Pb-Br-based solar cells. *ACS Appl. Mater. Interfaces* **2018**, *10*, 7145–7154. [CrossRef]